© 3rd IAHR Europe Congress, Book of Proceedings, 2014, Porto -Portugal. ISBN xxx-xxxx-xx-x

ON SPH MODELING OF SURF ZONE TURBULENCE UNDER WEAK PLUNGERS

CHRISTOS V. MAKRIS (1,A), CONSTANTINE D. MEMOS (2) & YANNIS N. KRESTENITIS(1,B)

(1) *Aristotle University of Thessaloniki, Thessaloniki, Greece,* A *cmakris@civil.auth.gr,* B *ynkrest@civil.auth.gr*

(2) *National Technical University of Athens, Athens, Greece, memos@hydro.ntua.gr*

Abstract

The aim of the present study is the numerical simulation of surf zone turbulence under weakly plunging waves on a relatively mild impermeable slope. Smoothed Particle Hydrodynamics method is implemented in combination with a Smagorinsky-type Sub-Particle Scale turbulence closure approach, similarly to Large Eddy Simulations. A combination of heuristic approaches for the discrimination of turbulent fluctuations from the ordered wave motion is proposed. Results in the surf zone concern wave-induced mean flows, turbulent characteristics of weak plungers and bores, coherent turbulent structures on vertical cross-sections, and intermittent events at fixed gauges. Their statistics agree with experimental data.

Keywords: SPH; weak plunging; surf zone turbulence; coherent turbulent structures; intermittent events

1. Introduction

Near-shore wave breaking is one of the most significant processes for coastal engineers and scientists in their endeavour to determine the surf and swash zone dynamics. Nevertheless, the highly turbulent nature of the respective transient flow regimes render the underlying hydrodynamics far from completely elucidated. For example, there is still no 'clean' definition of the turbulent characteristics or the discrimination of turbulent fluctuations from the ordered wave motion through certain averaging methods. There is still a lot of discussion taking place on the definition of coherent vortical or turbulent structures, and the description of intermittent (coherent or intense) turbulent events, which primarily control sediment movements and cross-shore morphodynamic evolution. In this direction, past research has concentrated mostly on the physical modeling, lately followed by three-dimensional (3D) numerical simulations of instantaneous and phase- or ensemble-averaged values of hydrodynamic quantities and fluid properties. Such factors are the free surface elevation η, the depth-averaged velocity U, the wave-induced mean flows (undertow and Stokes drift), the vorticity ω, the turbulent components of horizontal and vertical velocities u' and w' (i.e. $u=\bar{u}+u'$, u is fluid velocity and $\bar{u}$ is averaged velocity), the turbulent kinetic energy $k=(u'^2+w'^2)/2$, the turbulent shear and normal stresses $\tau_{ss}=\rho u'w'$ and $\tau_{nx}=\rho u'^2$ or $\tau_{nz}=\rho w'^2$ respectively (ρ is the fluid density), the topological characteristics of recurring vortical patterns, the characteristic turbulence length and time scales etc. The relations, provided above, concern the two-dimensional (2D) vertical case, which is the common rule for laboratory experiments of turbulence induced by spilling and plunging waves on inclined slopes.

The relevant studies are numerous, yet some of them are of specific importance for the present paper. Namely, Nadaoka et al. (1989) used Laser Doppler Velocimetry (LDV) for flow

visualizations and Eulerian velocity measurements to indicate that characteristic large-scale eddy structures under breaking waves transform from 2D structures with horizontal axes parallel to the crest line to 3D obliquely descending eddies (ODEs) behind the wave crest. ODEs seemed to be responsible for the Reynolds stresses near the free surface. Emerging vortical patterns, traced at the breaking wave front, were finally entrained through large-scale eddies into the underlying flow field. The separation of the irrotational velocity components (ordered wave motion) from the rotational mean velocity (eddy motion) was achieved through filtered phase-averaging of the velocity field. The generation of the vorticity field, related to the mean velocity component, caused considerable increase in mass and momentum transport and affected the wave height evolution in the surf zone. Cox and Kobayashi (2000) attempted LDV measurements of instantaneous values of u', w', τ_{ss} and k. They also traced the occurrence of coherent turbulent structures (CTS) through phase-averaging. Moreover, quadrant analysis of u' and w' helped define coherent motions, and conditional sampling techniques defined the statistics of coherent and intense events of intermittent nature. The authors concluded that the dominant vortices are of micro- or mid-size and of small life-span, yet carry up to nearly 50% of the total turbulent energy under the wave crest. Stansby and Feng (2005) used a large number of gauges, in order to investigate thoroughly the kinematics of the surf zone created by weakly plunging breaking waves. They thoroughly determined the recurrent vertical flow structures, including from large-scale motions down to small-scale vortical structures, through ensemble-averaging (Nadaoka et al., 1989). The multiple CTS just before and at the onset of breaking, led to elongated structures near and along the free surface during the turbulent bore propagation. Period-averaged ω, u and w were also obtained showing onshore mass transport above trough level against undertow-type backflow below it, while thick vorticity layers were observed at trough level and a thin one rotating oppositely near the bed.

On the other hand the Large Eddy Simulation (LES) approach shows up nowadays in numerical modeling of wave breaking turbulence. Relevant applications are numerous, yet some of them are referenced concisely, as important in the present study. Christensen and Deigaard (2001) used a Sub-Grid Scale (SGS) Smagorinsky-type model for the unresolved flow scales and depicted complicated flow phenomena such as ODEs. Christensen (2006) implemented LES to calculate the wave set-up, the undertow and turbulence features, yet for a rather coarse computational resolution, thus an overall overprediction of turbulence levels was found. Except from mesh-based LES methods, Smoothed Particle Hydrodynamics (SPH) (Monaghan, 2005) is widespread nowadays in the numerical modeling of free surface flows. Nonetheless, visually impressive SPH wave breaking simulations (Gómez-Gesteira et al., 2010b) somehow lack thorough affirmation concerning turbulent flow features. Shao and Ji (2006) proposed a LES-type SPH approach by using a Sub-Particle Scale (SPS) turbulence closure model. Results were good only in terms of η, u', and w'. In trying to fill the gap we test here state-of-the-art SPH against experiments for wave breaking in weak plunging form.

2. Methodology

SPH is a mesh-free particle method, based on Lagrange-type approximation of any given function $A(\mathbf{r})$ (scalar or vectorial) for Navier-Stokes equations, through integral interpolation smoothing (weighting) functions $W(\mathbf{r},h)$ (kernel), given in continuum and particle notation by:

$$A(\mathbf{r}) = \int A_j(\mathbf{r}')W(\mathbf{r}-\mathbf{r}',h)d\mathbf{r}' \Rightarrow A_i(\mathbf{r}) = \sum_j A_j\left(m_j/\rho_j\right)W_{ij} \quad [1]$$

where h is the smoothing length, m_j and ρ_j are the mass and the density of any particle j, W_{ij} is the kernel for partcle i in discretized notation, $\mathbf{r}$ and $\mathbf{r}'$ are the arbitrary particle position vector and the distance between particles i and j respectively. The SPH implementation used is the academic 'open source' numerical code SPHysics v.2 (Gómez-Gesteira et al., 2010a). Detailed assumptions regarding the choice of $W(\mathbf{r},h)$, boundary conditions treatment, numerical integration schemes, and in particular the SPS turbulence closure (Shao and Ji, 2006) can be found in our previous work (Makris et al., 2009; 2012).

3. Computational setup

3.1 Experimental data

The experiments of Stansby and Feng (2005) [SF05 hereafter] were chosen as a basis for the simulations presented below. The choice was driven by the compact size of the wave flume and the great variety of parameters investigated. A sketch of the wave flume setup is presented in Figure 1. The geometric and hydraulic features of the experiment are presented in SF05 and Makris et al. (2009). The surf similarity parameter (Irribaren number) at the breaking point $\xi_b = m_b/(H_b/L_0)^{1/2}$ of about 0.36, where m_b is the bottom slope, H_b the breaking wave height, and L_0 is the theoretical deep water wave length. The surf similarity parameter based on the initial wave height H (in front of the wavemaker) $\xi = m_b/(H/L_0)^{1/2}$ was about 0.46. These values of the Irribaren number are equidistant to 0.4, which is the boundary between spilling and plunging breakers (Battjes, 1974). The authors (SF05) stated that the waves obviously looked like they were breaking in weakly plunging form. The created water jet was almost totally reflected after hitting the forward trough. It was found that in the initial breaking phase, a cluster of eddies was formed in the water column with opposite direction of rotation. Thereafter the jet re-splashed several times and generated patterns of recurring coherent vortical structures, leading to the formation of a series of horizontally elongated eddies above trough level and near the free surface.

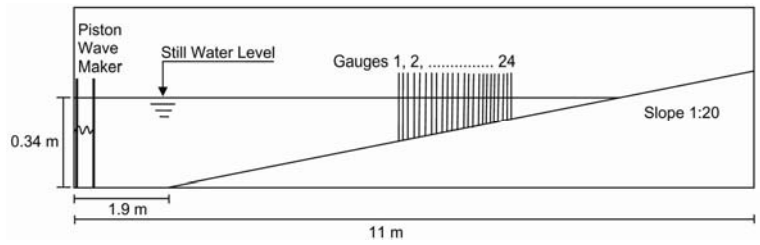

Figure 1. Sketch of the SF05 experimental setup.

3.2 Numerical wave flume

The size of numerical wave tank implemented for the SPH simulations was directly correspondent to the data provided by SF05 (Makris et al., 2009). Measurements of the turbulent hydrodynamic features were conducted at discrete numerical gauges in respect to the stations of SF05. The total number of numerical gauges used was 24, yet the horizontal

distances x_g from the wavemaker of only four characteristic ones are given in Table 1 together with the respective water depth d. Namely G8 and G10 were located in the incipient breaking region of the weak plunger, whilst G21 and G23 were placed in the inner surf zone.

Table 1. Horizontal distances of gauges from piston wavemaker (SF05).

Gauge	**G8**	**G10**	**G21**	**G23**
x_g (m)	5.540	5.737	6.796	7.200
d (m)	0.158	0.148	0.095	0.075

The sampling of fluid data from SPH simulations on fixed nodal points was achieved with a heuristic technique for the transformation of a Lagrangian hydrodynamic field to an Eulerian one. This relied on a spatial averaging procedure of any arbitrary fluid parameter A_n on a fixed computational node n, over its compact support domain of particles p. The technique was applied only on particles at the column of vertically discretized nodes that corresponded to gauges in SF05, in order to save computational time. In this framework, we used the following convolution integral in discrete particle notation (Farahani et al., 2012):

$$A_n = \sum_{p=1}^{N} A_p \cdot m_p / \rho_p \cdot W\left(\left|r_n - r_p\right|, h\right) \quad [2]$$

3.3 Analysis of flow scales

In order to select the proper spatial resolution Δx for the simulations, analysis of flow scales was undertaken. The length scales of turbulent motions, vortices and eddies could be divided into three categories. The first ones are the integral turbulence length scales λ_0, which correspond to the energy containing range of the flow. This range is relevant to the large eddies which include also the biggest part of the coherent vortical structures of the flow and correspond to the smallest wavenumbers of the turbulence energy spectrum (Pope, 2000). According to Cox et al. (1994) the mixing length is related to characteristic eddy sizes or λ_0 as:

$$\lambda_0 = \begin{cases} \kappa\left(z - z_0\right) & \text{for } z < z_{cr} = C_\lambda d/\kappa + z_0 \\ C_\lambda d & \text{for } z \geq z_{cr} = C_\lambda d/\kappa + z_0 \end{cases} \quad [3]$$

where κ is the Von Karman constant ($\kappa \approx 0.4$), z_0 is the bottom elevation, z is the vertical distance, z_{cr} is a critical value of z which determines the bottom boundary layer, d is the local water depth, and C_λ is a time-invariant empirical coefficient related to the eddy size. For the case of intensely spilling breaking waves Cox et al. (1994) calculated overall values of C_λ to be 0.04 outside the surf zone and at the incipient breaking region, 0.12 in the transition region in the mid surf zone and 0.18 in the inner surf zone. The upper limit of λ_0 is $\Lambda = 6 \cdot \lambda_0$ (Pope, 2000) and its value was calculated to vary between 25~100% of d. The lower limit of λ_0 is $\Lambda_{EI} = \lambda_0/6$ and sets the demarcation point between the anisotropic large eddies of length scales $\lambda > \Lambda_{EI}$ and the isotropic small eddies $\lambda < \Lambda_{EI}$ (Pope, 2000). Its value was found to range between 0.7~3% of d. The calculated percentages refer to the water column outside the boundary layer ($z \geq z_{cr}$) for the specific hydraulic and geometric features of the experiment implemented (SF05). Based on Eq. 4 we derived the values of $\lambda_0 \approx 5$~20 mm and $\Lambda_{EI} \approx 1$~3 mm throughout the entire surf zone. Λ_{EI} designates the boundary between λ_0 and the Taylor microscales λ_T. The latter are the second category of turbulent flow scales, i.e. the intermediate ones between the largest and the

smallest (Kolmogorov scales λ_K). They correspond to the inertial subrange of turbulence, where energy cascades to finer length scales without dissipation. The lower limit of λ_T is Λ_{DI} which discriminates them from λ_K that form the viscous sub-layer range, where energy is dissipated due to viscosity. All the above are schematically portrayed in Figure 2. In the simulations of the present study, the spatial discretization was chosen to be Δx=3 mm, thus turbulence in all flow scales below either λ_0 or in some cases Λ_{EI} was computed by the SPS model. Hence similarly to a LES approach the SPS-SPH model simulated explicitly the coherent turbulent structures and the large eddies in the energy containing range and modeled the turbulence in the inertial and dissipation ranges. Please note that we are far from a complete LES implementation in SPH, e.g. covering at least 80% of the flow scales and moving towards and beyond λ_T, especially for 'scalar' codes like SPHysics v.2. It is noted that simulations in the present study used up to more than $5.5 \cdot 10^5$ particles and involved 10~50 wave periods, to ensure that sufficient data would be obtained for statistical analysis of turbulence (Cox et al., 1994).

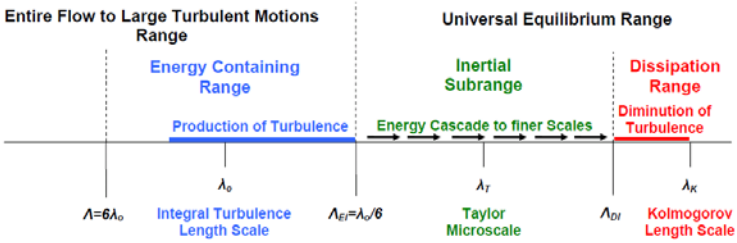

Figure 2. Diagram of turbulent flow length scales and eddy sizes.

4. Results

In a previous publication (Makris et al. 2012) we have shown that SPS-SPH model based on calibrated Smagorinsky coefficients (C_s=0.12~0.17) behaves plausibly in terms of the weak plunging depiction, the distribution of H and wave set-up throughout the entire domain, Eulerian measurements of η, ensemble-averaged and r.m.s. fluctuations of η or U, and various turbulent features in the surf zone, compared to the experimental results of SF05. In the present study we focus more on the period- or ensemble-averaged kinematics and the turbulent dynamics concerning the CTS at the incipient breaking region and the inner surf zone, through identification and discrimination of the large eddy motions from ordered wave motions and residual turbulence. Furthermore the instantaneous turbulent events are detected and studied through conditional probabilities. The derivation of CTS and recurring vortical patterns was based on the heuristic approach of ensemble-averaging by Nadaoka et al. (1989). It combined a moving average method (low-pass filter) for the tracing of residual turbulence with a phase-averaging operator for the raw velocity vector field $\mathbf{u}$, based on low-pass filtered $\tilde{\mathbf{u}}$:

$$\left\langle \mathbf{u}(\mathbf{x},\zeta t)\right\rangle = \frac{1}{N}\sum_{i=0}^{N-1}\tilde{\mathbf{u}}\left(\mathbf{x},\zeta\left(t+iT\right)\right) \qquad [4]$$

where ‹·› is the phase-average operator, i is the sample indicator, N is the maximum sample number equal to the simulated wave cycles (N=10~50), T is the wave period, ζ is the wave angular frequency, $\mathbf{x}$ is the position vector and t is the time interval of computations. The

turbulent fluctuations of the velocity vector field are given by $\mathbf{u}'=\mathbf{u}-\langle\mathbf{u}\rangle$. Thorough analysis of the moving-average sampling rates can be found in SF05.

4.1 Wave-induced mean flows

The vertical distribution of period-averaged velocity $\mathbf{u}_{\mathbf{mean}}$ vectors, at various gauges in the surf zone, is presented in Figure 3. The cross-shore return flow (undertow) and the shoreward mass transport flow (Stokes drift) are well predicted, compared to relevant depictions in SF05. These opposite wave-induced currents were clearly discerned by the wave trough and crest envelopes, whose evolution also revealed the propagating wave's advancing nonlinearity up to the breaking point. Moreover, even the shoreward inversion of the mean flow near the bed, called 'streaming', was reproduced qualitatively well, as shown by the onshore vectors of mean velocity in the bottom boundary layer. As an outcome, coherent rotational flow patterns emerged near the bed, as can be observed in vorticity maps further below. In order to check the counterbalancing effect of the undertow and the Stokes drift, the depth-integrated value of mean velocity was calculated and plausibly found to be practically zero ($F(\bar{\mathbf{u}})=<<0.01$ m^2/sec), with the use of the following relation: $F(\bar{\mathbf{u}})=\int \bar{\mathbf{u}}\, dz$.

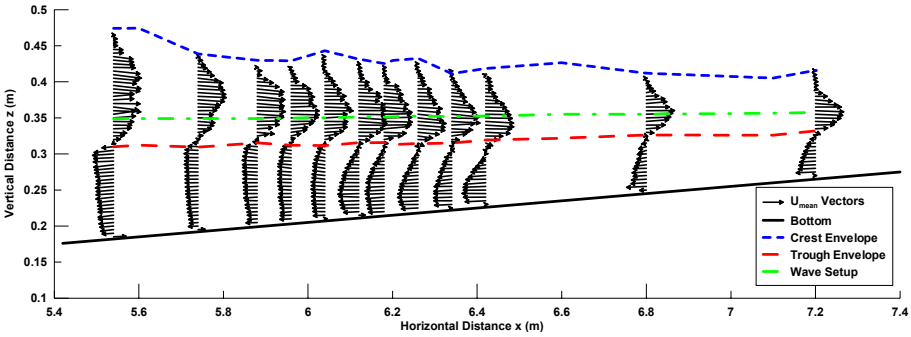

Figure 3. Period-averaged velocity vectors $\mathbf{u}_{\mathbf{mean}}$ at various gauges in the surf zone [upper graph]. Wave trough (red large-dash line), crest (blue small-dash line) and set-up (green dash-dot line) envelopes demarcate the undertow and Stokes drift regions.

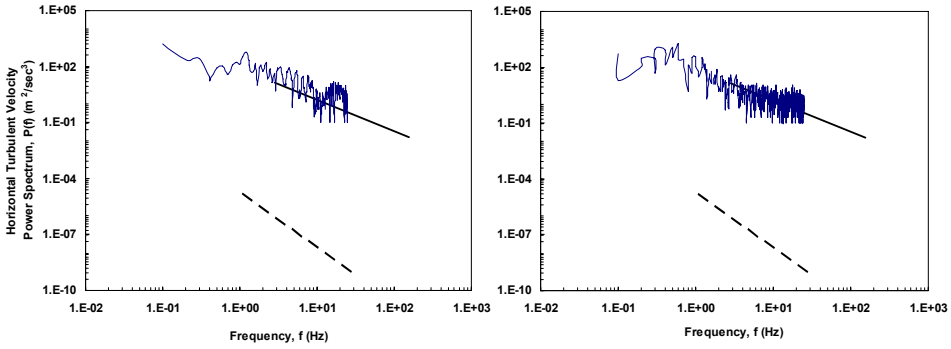

Figure 4. Fourier spectra $P(f)$ of simulated turbulent components of horizontal velocities u' for the incipient breaking region (G8) [left] and the inner surf zone (G23) [right], measured at still water level. -5/3 (full line) and -3 (dash line) gradients are shown. The Nyquist frequency from ensemble-averaging was f_N=25 Hz.

4.2 Turbulent flow properties of wave breaking

The Fourier power spectrum $P(f)$ of $\mathbf{u}'$ was derived at still water level in the incipient breaking region (G8) and the inner surf zone (G23) and are shown in Figure 4. Trends following the -5/3 gradient are obvious on the log/log scale, which is typical of isotropic (inertial sub-range) turbulence (Pope, 2000). The frequency range of isotropy was from f=1 Hz to at least the Nyquist filter limit f_N=25 Hz. Random turbulence below this frequency was lost in the averaging process. Thus the lower limit of the large-scale turbulent structures' life-span t_{cs} would practically be of the order of O(t_{cs})=1 sec, while turbulent energy cascade would involve coherent eddies with t_{cs} at most of the order of O(t_{cs})=0.04 sec. The -3 gradient, typical of 2D frozen turbulence, was also sketched on the graphs, yet it was never reproduced.

4.3 Coherent turbulent structures

For a 2D vertical plane of the hydrodynamic field, ω is always perpendicular to the flow and could be considered as a scalar field, given by $\omega=\partial u/\partial z-\partial w/\partial x$. In Figure 5, snapshots of the ω field are shown on a 2D vertical cross-section. Periodic patterns of concentrated ω (CTS) involve from large-scale vortices down to small-scale eddies. Specifically ω was large at the wave crest and the toe of the wavefront, and after the plunging jet formation it spread out over the whole surface roller region. The impingement and the rebound of the weak plunger on the forward trough actually induced topologically generated ω, independent of the wave-induced rotational flow. After that, multiple vortical structures descended obliquely to the bottom spreading also ω in the water column for a brief period after plunging, while the larger part of the vortices was permeated near the free surface, seaward of the broken wave crest. In the bore region vortical structures were stretched horizontally, just as reported by SF05. Anywhere else the flow was nearly irrotational, except from a thin layer of negative ω (counter-clockwise eddies) near the bed in front of the wave prior to breaking (SF05; Nadaoka et al., 1989). These CTS are most important in bed sediment pickup, suspension, and transport. Moreover the simulated ensemble-averaged vorticity $\langle\omega\rangle$ contour plots are shown in Figure 6 (upper graph), for the incipient breaking region and the inner surf zone, manifested as multiple CTS. At the plunging region they were concentrated near the crest and the bed, while at the turbulent bore region those structures were evidently spread mainly horizontally. Residual ω upstream of the incident bore was also apparent there, due to the passage of previous plungers (SF05). In the mid and lower graphs of Figure 6, equivalent results are presented for $\langle k\rangle$ and $\langle\tau_{ss}\rangle$, which are associated with the large coherent eddies of the flow ($l_{eddy}>\Delta x$). The temporal evolution of turbulence production and decay during the breaking process is actually illustrated for a wave period averaged over many cycles. TKE appeared just before breaking at the toe of the wavefront and grew during plunging, especially near the crest. Initial thin and dense layers of k were diffused with time, rendering them sparser, thicker and of lower energy at the wave tergum. TKE was convected from G8 to G23, with a fast dissipation rate within one wave period, and also reduced with depth, suggesting that turbulence transport dominated turbulence production below trough level. Furthermore k and ω were not correlated in some areas of the surf zone. In particular there were considerable amounts of turbulence produced by the plunging jet without the creation of CTS, and the residual vorticity after the passage of the wave was not accompanied by turbulence generation or conservation. The maximum of τ_{ss} was observed at the toe and the middle of the breaking wave front. In the bore region, values dropped to less than half of the initial ones, but with small background magnitudes residing

over the entire bore front, crest and back region. Hence the Reynolds stresses distribution appeared to have a peak value in the lower part of the eddy region at the wave trough level, where large amounts of vorticity were concentrated (Nadaoka et al., 1989). Thus the Reynolds stresses were produced mainly by the large-scale eddies and partly due to residual turbulence.

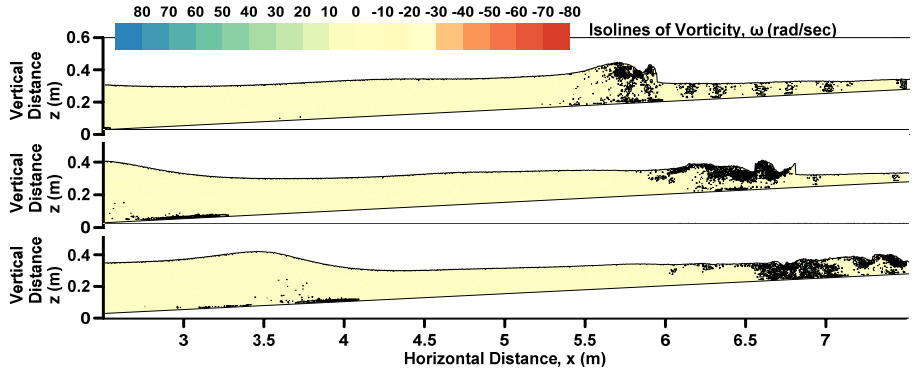

Figure 5. Simulated vorticity field ω (sec^{-1}) of large scale eddies under weak plunging breaking waves.

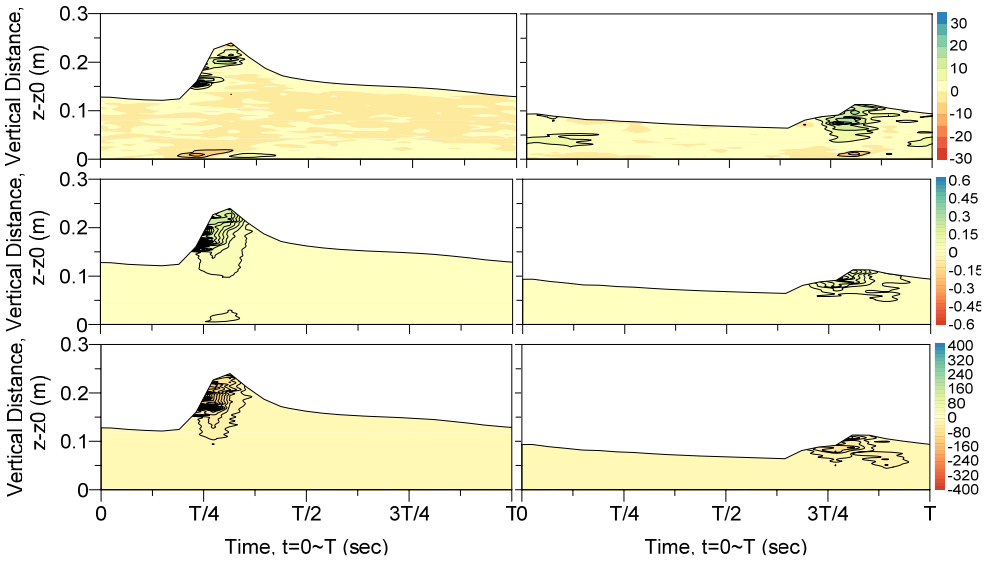

Figure 6. Simulated ensemble-averaged contour plots of vorticity ‹ω› (sec^{-1}) [upper graph], TKE ‹k› (m^2/sec^2) [mid graph], and turbulent shear stress ‹τ_{ss}› (Pa) [lower graph], for weak plungers at the incipient breaking region G8 [left graphs] and inner surf zone G23 [right graphs].

4.4 Intermittent turbulent events

Identification of intermittent events, both coherent and intense, was attempted according to Cox and Kobayashi (2000), by defining thresholds ($m+\sigma$ for coherent, $m+3\sigma$ for intense) based on the mean m and the standard deviation σ of the time-series of k and τ_{ss}. (Figure 7). Numerical measurements were taken at mid depth. The depth-averaged statistics of the coherent and intense events are presented in Table 2. It was found that intermittent coherent

[or intense] events of turbulence occur for a small portion N_{COH}<13% [or N_{INT}<4%] of the k and τ_{ss} time-series, but contribute significantly to their magnitude by containing a significant amount of all motions $(N{\cdot}m)_{COH}$>60% [or $(N{\cdot}m)_{INT}$>22%], in the entire surf zone. The relationship of these intermittent coherent and intense signals was examined with the use of conditional probabilities (not shown here). The correlation between τ_{ss} and k based coherent events decreases slightly as we go shoreward, while it increases for intense events. This indicates that the magnitude of the intense events increases landward in the surf zone, while the most frequent coherent events remain practically invariant. This is consistent with the breaking mechanisms and cross-shore sediment transport patterns of Cox & Kobayashi (2000).

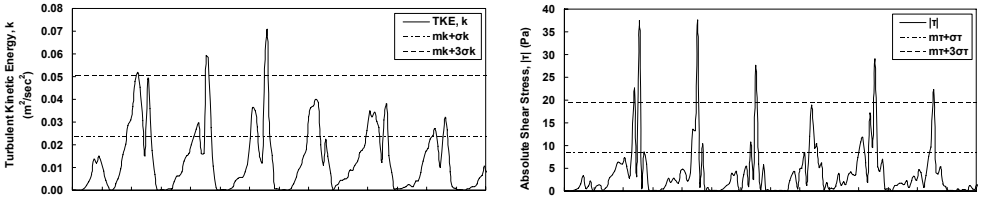

Figure 7. Identification of intermittent events based on temporal variation of TKE k (left graph) and of absolute shear stress $|\tau|$ (right graph), at mid-depth of the incipient breaking region (G8). Coherent and intense events thresholds are $m_k+\sigma_k$ and $m_k+3\sigma_k$ based on k; $m_\tau+\sigma_\tau$ and $m_\tau+3\sigma_\tau$ based on $|\tau|$.

Table 2. Detection of coherent and intense intermittent events and motions in depth-averaged percentages (%) using k (upper part) and $|\tau|$ (lower part).

	Coherent Events		**Intense Events**	
Gauge	N_{COH}/N (%)	$N_{COH}{\cdot}m_{k,COH}/N{\cdot}m_k$ (%)	N_{INT}/N (%)	$N_{INT}{\cdot}m_{k,INT}/N{\cdot}m_k$ (%)
G8	10.19	78.13	2.62	39.90
G10	8.54	74.38	1.65	47.69
G21	12.67	63.99	2.20	22.85
G23	9.50	61.09	1.79	26.72
Gauge	N_{COH}/N (%)	$N_{COH}{\cdot}m_{\tau,COH}/N{\cdot}m_\tau$ (%)	N_{INT}/N (%)	$N_{INT}{\cdot}m_{\tau,INT}/N{\cdot}m_\tau$ (%)
G8	7.02	73.19	2.07	41.67
G10	5.92	69.25	2.20	49.65
G21	10.19	63.07	1.93	24.61
G23	7.85	64.14	3.17	40.09

5. Conclusions

A refined resolution SPH model was implemented, combined with a Smagorinsky-type SPS approach for turbulence closure, in order to simulate the period-averaged kinematics, ensemble-averaged, and instantaneous turbulence in the surf zone created by a weak plunger, similarly to the experimental endeavour of Stansby and Feng (2005). A combination of heuristic methods was proposed for the transformation of the scattered Lagrangian SPH data to Eulerian values at fixed nodal points (gauge locations), and the discrimination of CTS and intermittent events from ordered wave motions through ensemble-averaging. Thorough analysis of the flow length scales was presented and the mixing lengths of the flow (Cox et al., 1994) defined the limit of Δx for a LES approach in SPH. The wave-induced mean flows were

qualitatively well reproduced compared to experiments. Simulations clearly portrayed the undertow and Stokes drift regions, as well as 'streaming' near the bottom. The calculated fluxes over a wave period confirmed a naught balance of the cross-shore currents. Fourier spectra of turbulent velocities revealed isotropy of turbulence up to rather high frequencies. SPS-SPH satisfactorily reproduced CTS and large-scale repetitive vortical patterns compared to experiments. Entrainment of vorticity by large-scale eddies from the wavefront into the underlying field was observed (Nadaoka et al., 1989), inducing elongated vortical layers along the surface of the bore. Negative vorticity CTS were derived near the bed, similar to a mixing layer. Analysis of turbulence intermittency in the surf zone revealed that coherent (intense) events occur approximately for 10% (3%) of the record but account for 60% (20%) of the total number of motions. Statistics clearly indicate the infrequency of these motions, yet they are of great significance in contributing to turbulence, shear stresses and to sediment transport.

References

Battjes J.A. 1974. 'Surf similarity', *Proc. 14th Int. Conf. on Coast. Eng.*, 466-480.

Christensen E.D., Deigaard R. 2001. 'Large eddy simulation of breaking waves', *Coast. Eng.*, 42, 53-86.

Christensen E.D. 2006. 'Large eddy simulation of spilling and plunging breakers', *Coast. Eng.*, 53, 463-485.

Cox D.T., Kobayashi S. 2000. 'Identification of intense, intermittent coherent motions under shoaling and breaking waves', *J. of Geophys. Res.*, 105(C6), 14223-14236.

Cox D.T., Kobayashi N., Okayasu A. 1994. 'Vertical Variations of Fluid Velocities and Shear Stress in Surf Zones', *Proc. 24th Int. Conf. Coast. Eng.*, 98-112.

Farahani R.J., Dalrymple R.A., Hérault A., Bilotta G. 2012. 'SPH modeling of mean velocity circulation in a rip current system', *Proc. 33rd Int. Conf. on Coast. Eng.*

Gómez-Gesteira M., Rogers B.D., Dalrymple R.A., Crespo A.J.C., Narayanaswamy M. 2010a. 'User Guide for the SPHysics Code v2.0'.

Gómez-Gesteira M., Rogers B.D., Dalrymple R.A., Crespo A.J.C. 2010b. 'State-of-the-art of Classical SPH for Free-Surface Flows', *J. of Hydr. Res.*, 48, Extra Issue, 6-27.

Makris C.V., Memos C.D., Krestenitis Y.N. 2009. 'Numerical Simulation of Near-Shore Wave Breaking using SPH Method', *Proc. of 4th Int. Short Conf. on Applied Coast. Res.*, Barcelona, Spain, 15-17 June 2009, 241-252.

Makris C.V., Krestenitis Y.N., Memos C.D. 2012. 'SPH modeling of plunging wave breaking, surf zone turbulence and wave-induced currents', *Proc. of 22nd Int. Offshore (Ocean) and Polar Eng. Conf.*, ISOPE, Rhodes, Greece, 17-22 June 2012, 1204-1212.

Monaghan J.J. 2005. 'Smoothed Particle Hydrodynamics', *Rep. Prog. Phys.*, 68, 1703-1759.

Nadaoka K., Hino M., Koyano Y. 1989. 'Structure of the Turbulent Flow Field Under Breaking Waves in the Surf Zone', *J. Fluid Mech.*, 204, 359-387.

Pope S.B. 2000. 'Turbulent Flows', Cambridge University Press.

Shao S., Ji C. 2006. ,SPH Computation of Plunging Waves Using a 2-D Sub-Particle Scale (SPS) Turbulence Model', *Int. J. Numer. Meth. Fluids*, 51, 913-936.

Stansby P.K., Feng T. 2005. 'Kinematics and Depth-Integrated Terms in Surf Zone Waves from Laboratory Measurement', *J. Fluid Mech.*, 529, 279-310.